ARTICLE

SCIENCE CHINA Earth Sciences 2026 69(3): 1107–1117
earth.scichina.com link.springer.com
https://doi.org/10.1007/s11430-025-1851-7

Oblique convergence drives left-lateral slip on the Altyn Tagh Fault: Evidence from crustal anisotropy

Chenglong WU[1], Tao XU[1*], Jiyan LIN[2], Tongtong XIE[1,3], Xiaobo TIAN[4] & Zhanwu LU[5]

[1] Key Laboratory of Deep Petroleum Intelligent Exploration and Development, Institute of Geology and Geophysics, Chinese Academy of Sciences, Beijing 100029, China
[2] Geophysical Exploration Center, China Earthquake Administration, Zhengzhou 450002, China
[3] Qingdao Institute of Marine Geology, China Geological Survey, Qingdao 266237, China
[4] State Key Laboratory of Lithospheric and Environmental Coevolution, Institute of Geology and Geophysics, Chinese Academy of Sciences, Beijing 100029, China
[5] Institute of Geology, Chinese Academy of Geological Sciences, Beijing 100037, China

* Corresponding author (email: xutao@mail.iggcas.ac.cn)

Received 14 October 2025; Revised 8 January 2026; Accepted 23 January 2026; Published online 6 February 2026

Abstract The Altyn Tagh Fault (ATF) system separates the Tibetan Plateau from the Tarim Basin and accommodates the northeastward expansion of the plateau. However, crustal deformation across the ATF remains poorly studied, limiting our understanding of the mechanisms driving plateau uplift and expansion. Using data from a short-period dense array across the ATF system and nearby permanent stations, we determined the crustal anisotropy by fitting the sinusoidal moveout of Pms phases in receiver functions. This approach provides key constraints on intracontinental deformation features. The average fast directions of crustal anisotropy are ENE-WNW in the eastern Tarim Block, nearly E-W in the Altyn Tagh Range (ATR), and NW-SE in the Qaidam Block, corresponding to average splitting times of 0.42, 0.61, and 0.68 s, respectively. In the eastern Tarim Block, the crustal anisotropy aligns with paleotectonic structures, reflecting fossil anisotropy preserved within the craton. The southward underthrusting of the Tarim Block and the NNE-NE extrusion of the northern Tibetan Plateau have generated pure-shear deformation within the crust beneath the northern ATR and the western Qaidam Basin, respectively, producing corresponding E-W and NW-SE crustal anisotropy. The oblique convergence between the Tarim Block and the Tibetan Plateau facilitates left-lateral strike-slip shearing along the central segment of the ATF as well as transpressional deformation within the ATR. This process has driven the uplift of the ATR and accommodated the outward extrusion of plateau material, thereby dominating the intracontinental deformation pattern across the northern margin of the Tibetan Plateau.

Keywords Tibetan Plateau, Altyn Tagh Fault, Intracontinental deformation, Receiver function, Crustal anisotropy

1. Introduction

The continuous collision and compression of the Indian and Eurasian plates during the Cenozoic have given rise to the vast Tibetan Plateau and triggered the reactivation of boundary faults, including the Altyn Tagh Fault (ATF) (Yin and Harrison, 2000). Stretching over 1,500 km, the ATF system ranks among the Earth's largest strike-slip fault systems. It defines the northern boundary of the Tibetan Plateau, separating the Tarim and Qaidam basins (Tapponnier and Molnar, 1977). It accommodates a quarter to half of the India-Siberia convergence via left-lateral slip (Avouac and Tapponnier, 1993; Shen et al., 2001). This makes it a crucial boundary in various dynamic models of plateau uplift and expansion (Yue and Liou, 1999; Tapponnier et al., 2001; Yin et al., 2002). Quaternary geomorphology, GPS and InSAR studies consistently document a slip rate around 10 mm yr^{-1} in the central ATF, which decreases eastward to less than 1 mm yr^{-1} at its eastern terminus (Cowgill, 2007; Zhang et al., 2007; Chen Y W et al., 2013; Li et al., 2018). While these observations constrain shallow crustal motion, they offer limited direct constraints on deformation at depths. Thus, investigating deep intracontinental deformation within and around the ATF system is crucial for understanding the formation and evolution of the Tibetan Plateau's northern margin, as well as the mechanisms driving the plateau's uplift and expansion.

Seismic anisotropy serves as the most direct indicator of crust-mantle deformation and remains a key tool for probing the Earth's interior deformation (Silver and Chan, 1991; Gao, 2005). Using a portable seismic array across the ATF, Herquel et al. (1999) conducted XKS splitting analysis and concluded that left-lateral shear governs the deformation inside the fault zone and accommodates NE extrusion of the Tibetan Plateau. Integrating XKS splitting and surface deformation data, Chang and Wang (2023) revealed that crust-mantle decoupling beneath the Tarim Basin, contrasting with the vertically coherent lithospheric deformation observed in northern Tibetan Plateau and the southeastern Tarim margin. However, XKS splitting measurements integrate anisotropy along the entire S-wave path from the core-mantle boundary to the surface; they primarily reflect upper mantle deformation and thus offer limited direct constraints on the crust. Consequently, in the intensely deforming boundary zones of the Tibetan Plateau, measurements of crustal anisotropy become essential. They provide critical insights into crustal

Citation: Wu C, Xu T, Lin J, Xie T, Tian X, Lu Z. 2026. Oblique convergence drives left-lateral slip on the Altyn Tagh Fault: Evidence from crustal anisotropy. Science China Earth Sciences, 69(3): 1107–1117, https://doi.org/10.1007/s11430-025-1851-7

deformation and act as key evidence for deciphering crust-mantle deformation mechanisms.

With its raypath confined to the crust, the Pms converted phase of the Moho discontinuity serves as an ideal seismic phase for probing crustal deformation (Chen Y et al., 2013). Using a portable array in northern Xizang, Herquel et al. (1995) applied Pms splitting analysis to reveal eastward material extrusion of the Tibetan Plateau. However, because Pms phases from individual events typically have low Signal-to-Noise Ratios (SNR), obtaining splitting parameters as robust as those from XKS phases remains challenging. To address this issue, the analysis of back-azimuthal variations in Pms phases from receiver functions provides a robust alternative (Liu and Niu, 2012; Rümpker et al., 2014). Consequently, this approach has seen growing application in studies of crustal deformation within and around the Tibetan Plateau. In central, western, and southeastern Xizang, crustal anisotropy results are commonly attributed to middle-lower crustal flow (Sun et al., 2012; Wu et al., 2015; Kong et al., 2016; Zheng et al., 2018; Wu C et al., 2019; Nie et al., 2023; Shi et al., 2023). Conversely, in the northeastern plateau, integrated analyses of crustal anisotropy and XKS splitting predominantly favor crust-mantle coupling and vertically coherent lithospheric deformation (Wang et al., 2016; Xu et al., 2018; Guo et al., 2019). Given the scarcity of crustal anisotropy constraints in the northern Tibetan Plateau and central ATF zone, this study systematically derives anisotropy results for the region by analyzing the sinusoidal moveout of Pms phases in receiver functions. These findings provide new, direct constraints on intracontinental deformation and the deep dynamics of plateau uplift and expansion.

2. Geological setting and current research progress on deep structures

The Altyn Tagh Fault system comprises the ENE-striking, left-lateral ATF and the NE-trending North Altyn Fault (NAF) north of its central segment (Cowgill et al., 2003). Together with the Jinyanshan Fault that lies northeast of the NAF, these structures bound the rhombus-form Altyn Tagh Range (ATR) (Fig. 1; Wu L et al., 2019). Situated north of the ATF system, the Tarim Basin is underlain by a Precambrian basement generated through the Paleoproterozoic amalgamation of the North Tarim and South Tarim Blocks (Yang et al., 2018). The Tarim Cenozoic strata have not undergone significant deformation (Laborde et al., 2019). Mantle plume activity beneath the Tarim Block intensified in the Early Permian, thereby enhancing the lithospheric strength of the Tarim (Xu et al., 2014). Ambient noise tomography reveals low-velocity anomalies in the Cenozoic sedimentary layer of the Tarim Basin, underlain by high-velocity middle-lower crust. These features point to a stable, craton-type rigid structure beneath the basin (Tan et al., 2023). South of the ATF system, the Qaidam Basin is underlain by a Proterozoic-Paleozoic basement. Its southern and northern margins are characterized by abundant WNW-NW-trending thrust faults, which formed in response to the NNE-directed compression generated by the Indo-Eurasian continental collision (Wang et al., 2012).

Geophysical observations across the Tibetan northern boundary consistently indicate underthrusting of the Tarim lithosphere beneath the ATR, although its geometry and the deep extension of the ATF remain debated. A wide-angle reflection/refraction profile shows a flat Moho beneath the ATF, suggesting the fault is confined to the crust and that the Tarim lithosphere underthrusts from NE to SW (Zhao et al., 2006). In contrast, body-wave tomography reveals southward subduction of the Tarim crust to ~150 km depth and interprets the ATF as a transcrustal fault (Wittlinger et al., 1998), with supporting evidence from magnetotelluric studies (Zhang et al., 2015). Recent receiver function Common Conversion Point (CCP) imaging and wave-field modeling using a dense array across the ATF system reveal underthrusting of the Tarim lower crust to ~75 km depth beneath the ATR, accompanied by partial eclogitization and a >20 km Moho offset beneath the ATF (Wu et al., 2024). The high-resolution crustal structure is generally consistent with other receiver-function studies in the region (Shi et al., 2007; Wang et al., 2024). Meanwhile, relatively low velocity and electrical resistivity in the middle-lower crust support the existence of crustal flow in the westernmost Qaidam (Zhao et al., 2006; Zhang et al., 2015). This interpretation, however, conflicts with the vertically coherent lithospheric deformation model proposed by Chang and Wang (2023). Crustal anisotropy studies thus offer key constraints to discriminate between these competing deformation models.

3. Data and methods

This study integrates two distinct datasets: a short-period dense seismic array deployed across the ATF and regional permanent broadband stations in northern Xizang (Fig. 1). The short-period array operated from September to November 2021, providing two months of continuous seismic waveform data (Wu et al., 2024). The profile spans approximately 430 km, and the average station spacing is 0.9 km. We incorporated continuous recordings from 10 permanent stations between December 2019 and December 2021 to improve station coverage. Teleseismic events with magnitudes $\geqslant$5.5 and epicentral distances between 28° and 95° were selected for Receiver Function (RF) analysis (Fig. 2).

3.1 Calculation of RFs

For the short-period dense array data, we rotated the horizontal components into radial and transverse components. Next, we used the time-domain iterative deconvolution method to compute radial RFs (Ligorría and Ammon, 1999), adopting a Gaussian coefficient of 5.0. After manual quality control, a total of 7013 high-quality RFs from 41 events were retained. These RFs were extracted from Wu et al. (2024). The same processing flow was applied to broadband seismic data, except that a Gaussian coefficient of 2.5 was used to better retain lower-frequency signals. This yielded 2396 high-quality RFs from 389 events after manual selection (Fig. 2). Although crustal anisotropy can also be estimated from azimuth-weighted stacking of transverse RFs (Shen et al., 2015; Qiang et al., 2019; Wu et al., 2021), the transverse components from short-period stations—the primary data source in this study—exhibit low SNRs. Therefore, only radial RFs were employed in the subsequent anisotropy analysis.

3.2 RF moveout correction and multi-station stacking

All receiver functions underwent moveout correction to a

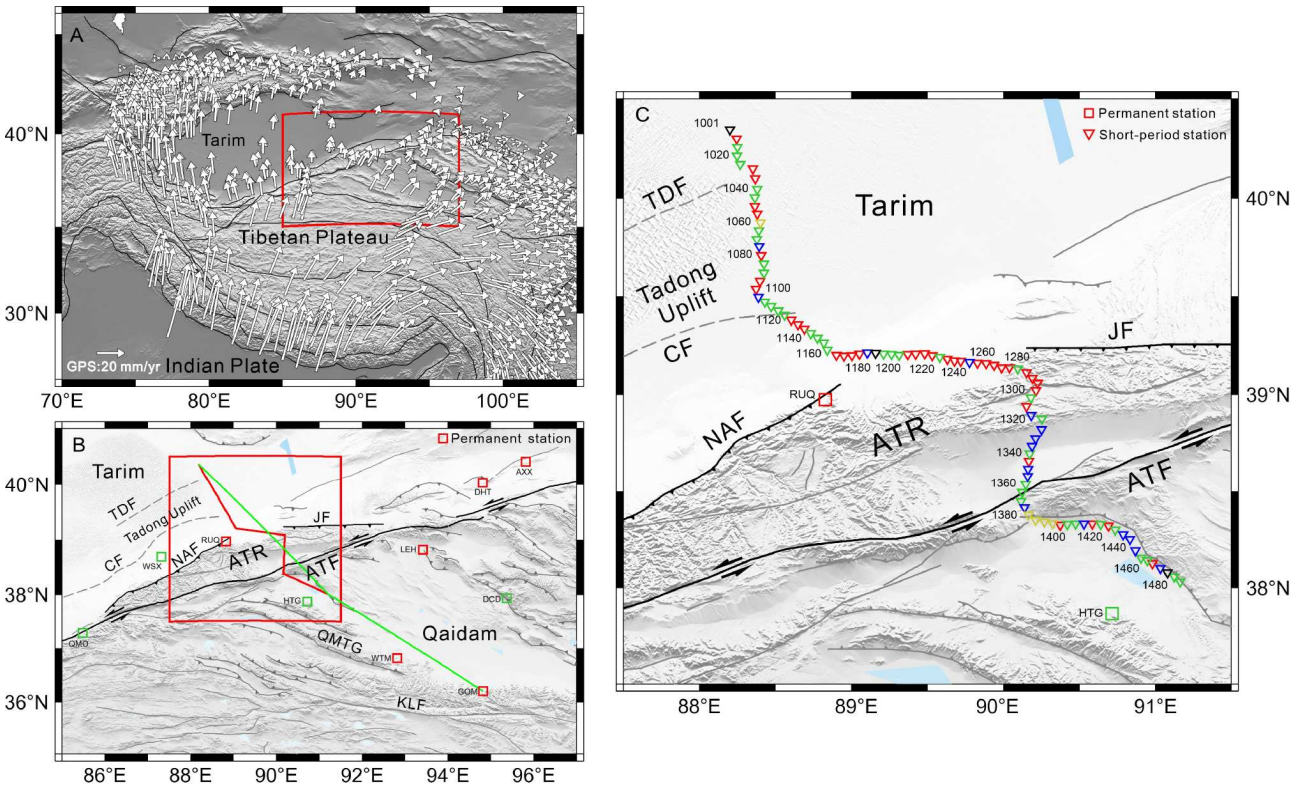

Fig. 1 Tectonic background and station distribution in the study area. (A) Location of the study area (red box) within the Tibetan Plateau. The GPS velocity field is represented by white arrows (Wang et al., 2020). (B) Close-up view: the red zigzag line marks the short-period dense array; red squares indicate permanent broadband stations; the green line shows the projected profile of the crustal anisotropy results; the red box indicates the short-period array deployment area detailed in (C). (C) Station layout: inverted triangles stand for short-period stations, and squares represent permanent stations with labels. Major tectonic features: NAF, North Altyn Fault; ATF, Altyn Tagh Fault; JF, Jinyanshan Fault; CF, Cherchen Fault; TDF, Tadong Fault; KLF, Kunlun Fault; QMTG, Qimantag Fault. In Figs. (B) and (C), the red stations represent those whose crustal anisotropy parameters meet the standard criteria (as explained in Section 3.4). The green stations indicate stations with significant discrepancies between the two methods. The blue stations denote stations with large standard deviations in crustal anisotropy parameters. The yellow stations correspond to stations with insufficient back-azimuth coverage. The black stations represent stations exhibiting weak anisotropy.

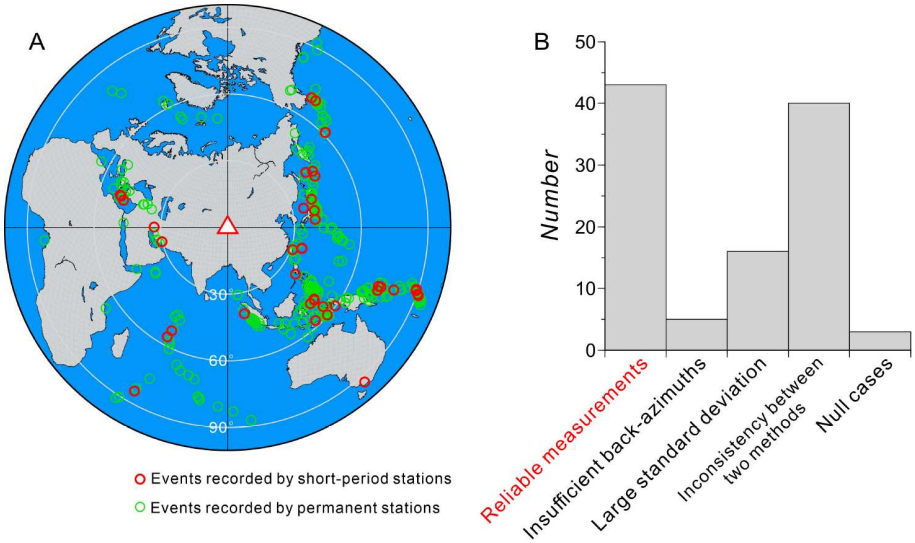

Fig.2 Distribution of teleseismic events and classification of crustal anisotropy measurements. (A) Teleseismic events used for the short-period dense array (red circles) and permanent stations (green circles). (B) Classification of all obtained crustal anisotropy measurements. A total of 43 pairs of reliable splitting parameters were retained.

reference slowness of 0.06 s km^{-1} to eliminate the effects of varying epicentral distances. The velocity model employed for moveout correction was constructed based on the velocity structure acquired through the wide-angle reflection/refraction profile (Zhao et al., 2006) and tectonic subdivisions. We divided the model into 5 regions in total, with the *Vp*/*Vs* ratio for each region determined from the regional average results of *H*-*κ* stacking of RFs (Wu et al., 2024). Individual short-period

stations recorded only a limited number of teleseismic events, resulting in poor back-azimuthal coverage. To address this, we applied the central station stacking method (Wu et al., 2023). This method stacks RFs from 11 neighboring stations—five on either side along the array—onto a central station, with the process repeated every five stations. Thereby, it coherently combines teleseismic signals recorded within a ~5 km radius. To enhance the SNR of RFs and mitigate the influence of uneven back-azimuth distribution, we stacked and averaged traces within each 10° back-azimuth bin. Most teleseismic events recorded by the short-period stations originated from the SE back-azimuth, with additional events distributed across the other three quadrants. Despite the limited number of events, high-quality RFs were yielded that enable robust crustal anisotropy analysis. Permanent stations recorded events from a fairly even distribution of back-azimuths.

3.3 Estimation of crustal anisotropy

For single-layer crustal anisotropy featuring a horizontal symmetry axis, the Pms arrival in radial RFs follows a cos2α variation with back-azimuth, exhibiting a four-lobe pattern (eq. (1); Liu and Niu, 2012). This method has been widely adopted in recent years for measuring crustal anisotropy, which is characterized by the fast-wave direction (φ) and the splitting time (δt) between the fast and slow waves. However, Moho inclination also impacts the Pms phase by imparting systematic arrival-time and amplitude variations that follow a cosα function (Li et al., 2019; Tan and Nie, 2021; Yang et al., 2022). Given the complex Moho geometry and intense tectonic deformation in the ATF system and northern Xizang, we adopted two fitting approaches to the Pms arrivals on the radial RFs—one using only the cos2α function, and the other incorporating both cosα and cos2α components (Zhang et al., 2022).

$$t = t_0 + \Delta t = t_0 - \frac{\delta t_{\mathrm{Pms}}}{2}\cos\left[2(\alpha - \varphi_{\mathrm{Pms}})\right] \quad (1)$$

$$t = t_0 + \Delta t = t_0 + \frac{\delta t_1}{2}\cos(\alpha - \varphi_1) - \frac{\delta t_{\mathrm{Pms}}}{2}\cos\left[2(\alpha - \varphi_{\mathrm{Pms}})\right] \quad (2)$$

where t_0 denotes the Pms arrival time in an isotropic medium; Δt represents the travel-time difference caused by crustal anisotropy along the ray path beneath the station; α stands for the back-azimuth of the RF; δt_{Pms} and φ_{Pms} denote the splitting time and fast direction, respectively, which characterize crustal anisotropy; δt_1 and φ_1 correspond to the two-lobe variation and are associated with the Moho dip. The optimal pair of anisotropy parameters was determined through a grid search for t_0, δt_{Pms}, and φ_{Pms} (with δt_1 and φ_1 included for eq. (2)) that yields the maximum stacked amplitude of the predicted Pms phases in the RFs. The search ranges were as follows: t_0 covered all Pms phases on the back-azimuth profile; φ_1 and φ_{Pms} were scanned from 0°–360° and 0°–180°, respectively, both with a 2° step; δt_1 and δt_{Pms} were searched from 0 to 1.5 s at a step of 0.05 s. Uncertainties were estimated using bootstrap resampling technique (Efron and Tibshirani, 1986). Figs. 3 and 4 show example anisotropy results for a short-period central station 1260 and a permanent station RUQ, both situated on the northern margin of the ATR. The strong agreement between the anisotropy parameters derived from the two station types validates the reliability of the short-period station measurements.

3.4 Selection criteria

Synthetic tests demonstrate that the fitting method employing eq. (2) produces more stable estimates of crustal anisotropy. Consequently, the results derived from this approach were adopted as the final solutions (Zhang et al., 2022, 2023). To ensure result reliability, the following quality criteria were applied: (1) adequate back-azimuth coverage, requiring more than 12 azimuth bins (10° per bin) and a maximum back-azimuth gap less than 180° (Zheng et al., 2018); (2) the Standard Deviation (*SD*) of anisotropy parameters less than 0.4 (the *SD* definition follows Kong et al., 2016); (3) good consistency between anisotropy parameters from the two methods, with differences of less than 30° in fast direction and less than 0.3 s in splitting time (Zhang et al., 2022); (4) splitting times below 0.2 s were categorized as null measurements (Xu et al., 2018).

4. Results

Reliable crustal anisotropy measurements were successfully obtained from 37 out of 97 short-period central stations and 6 out of 10 permanent stations (Fig. 2; Table 1). The region exhibits an average fast direction of roughly E-W, and the average splitting time is 0.57±0.25 s. Crustal anisotropy typically originates from either preferentially aligned microcracks in the upper crust or the lattice-preferred orientation of anisotropic minerals in the middle-lower crust (Rabbel and Mooney, 1996; Sun et al., 2024). Results from the surrounding Tianshan Mountains and the northeastern Tibetan Plateau show that upper-crustal anisotropy contributes to splitting times on the order of 0.1 s or less (Guo et al., 2015; Li et al., 2021). Thus, we conclude that the observed anisotropy likely originates dominantly from the middle-lower crust.

Within the eastern Tarim Block, the fast direction is predominantly ENE-WSW, and the average splitting time is 0.42±0.25 s. The crustal anisotropy is in line with tectonic structures such as the Tadong and the Cherchen Faults. In the ATR region, the fast direction is mainly near E-W, with an average anisotropy of 0.61±0.19 s, and runs roughly parallel to local tectonic trends. Clear Pms phases were detectable only at two central stations (1365 and 1400), with most short-period stations yielding no usable signal. Despite its location on the westernmost boundary of the Qaidam Basin, the ENE-oriented crustal anisotropy at station 1400 appears to be governed primarily by the strike-slip motion of the ATF. Further support comes from receiver-function CCP imaging, which reveals that the fault dips and extends southward beneath the station (Wu et al., 2024). In contrast, the Qaidam Block exhibits a distinct NW-SE fast direction with a mean splitting time of 0.68±0.33 s. At all stations, except for the central station 1465, the fast direction is generally consistent with the strike of nearby thrust faults.

5. Discussion

5.1 Fossilized crustal anisotropy in the eastern Tarim Block

The nearly horizontal Cenozoic strata in the Tarim Basin indicate negligible Cenozoic deformation (Laborde et al., 2019; Xie et al., 2023). Thus, the observed crustal anisotropy likely represents a fossil record of ancient major geological events (Fig. 5). Within

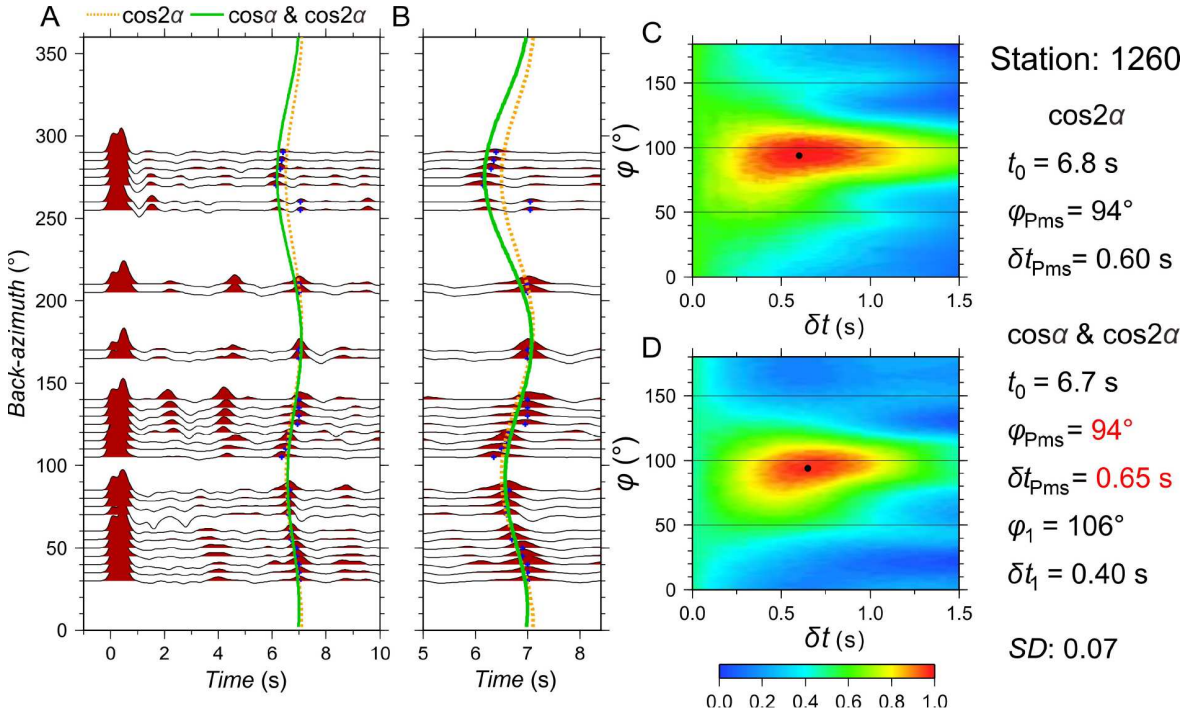

Fig. 3 Crustal anisotropy results for the short-period central station 1260. (A) Back-azimuth-averaged RFs. Blue crosses mark the Pms arrivals; orange dashed line and green solid line represent the theoretical moveout curves predicted by eqs. (1) and (2), respectively. (B) Zoomed-in view of the RF waveforms around the Pms arrivals. (C, D) Stacking-amplitude maps for all pairs of anisotropy parameters based on eqs. (1) and (2), respectively; the black dots mark the optimal anisotropy parameter pairs corresponding to the maximum stacked amplitudes. The right panel shows the crustal anisotropy parameters, with the final solution highlighted in red.

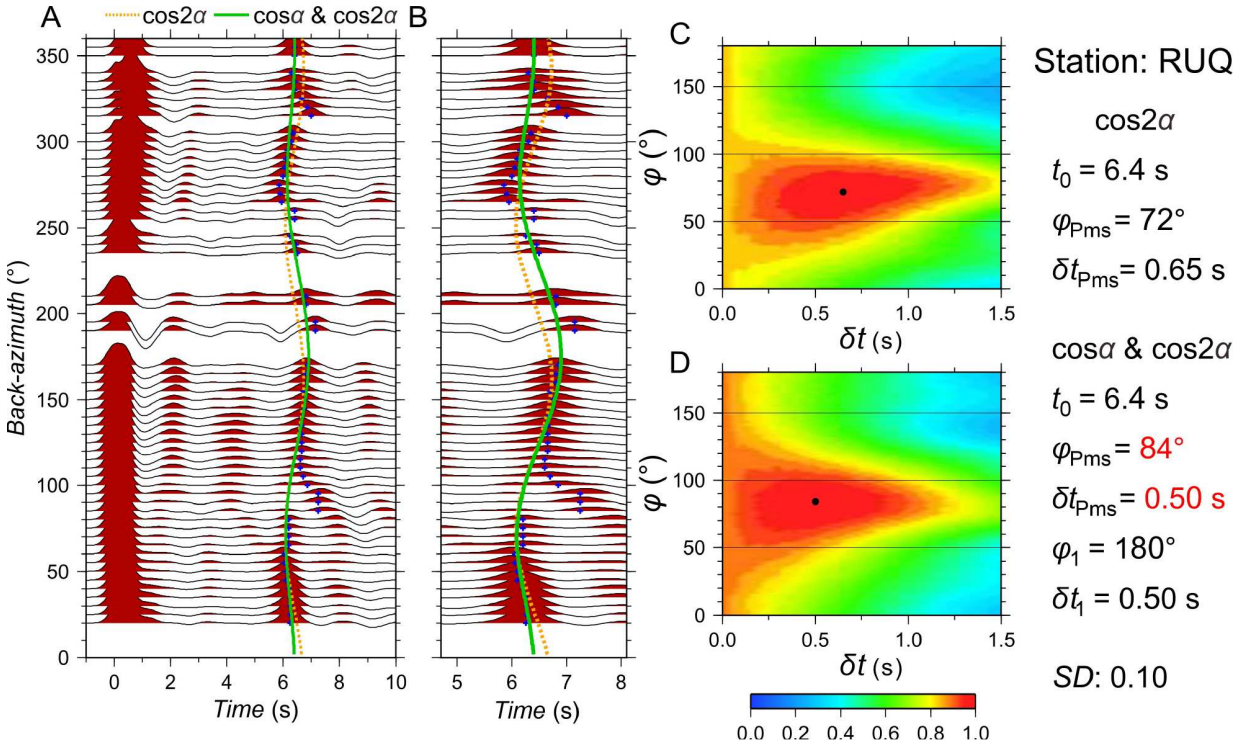

Fig. 4 Crustal anisotropy results for the permanent broadband station RUQ. All conventions follow those used in Fig. 3.

the Tarim Basin, the Central Tarim Terrain (CTT) is identified by a prominent aeromagnetic anomaly belt near ~40°N and separates the Southern and Northern Tarim Blocks (Yang et al., 2012). The widespread ~1.9 Ga magmatism within the CTT suggests that this terrain is an orogenic belt that resulted from the amalgamation of the Southern and Northern Tarim Blocks

Table 1 Reliable measurements of crustal anisotropy[a)]

Station	Lon (°E)	Lat (°N)	φ (°)	φ_{err} (°)	δt (s)	δt_{err} (s)	*SD*	No. of events
1010	88.2456	40.298	20	4.5	0.20	0.05	0.10	35
1030	88.3517	40.1493	106	11.5	0.25	0.11	0.24	35
1035	88.3681	40.0989	64	2.2	1.00	0.13	0.15	34
1050	88.3641	39.9585	86	1.8	0.60	0.05	0.07	34
1055	88.3806	39.9209	78	1.8	0.60	0.09	0.11	30
1080	88.4071	39.7081	132	9.9	0.20	0.05	0.16	34
1095	88.3983	39.5774	114	9.2	0.65	0.12	0.22	33
1100	88.3728	39.537	112	8.4	0.30	0.06	0.15	34
1130	88.6038	39.3806	84	6.6	0.30	0.04	0.12	37
1135	88.6476	39.3571	68	6.6	0.35	0.07	0.14	37
1140	88.6904	39.334	62	5.7	0.20	0.04	0.10	37
1165	88.902	39.1998	86	5.1	0.65	0.15	0.21	33
1170	88.9518	39.1968	92	9.3	0.55	0.11	0.21	30
1175	89.0043	39.1985	96	10.2	0.50	0.07	0.18	29
1180	89.0532	39.2058	86	8.9	0.50	0.12	0.22	30
1210	89.3693	39.2038	104	2.0	0.25	0.02	0.05	38
1215	89.422	39.206	106	5.6	0.45	0.04	0.10	37
1220	89.4823	39.2078	106	1.6	0.45	0.05	0.06	37
1225	89.5324	39.1986	90	5.8	0.65	0.03	0.10	36
1235	89.6311	39.1803	124	11.0	0.55	0.07	0.20	36
1240	89.6769	39.1728	106	3.2	0.55	0.06	0.10	36
1245	89.7196	39.1694	86	3.2	1.25	0.19	0.22	35
1255	89.8287	39.1609	104	4.9	0.70	0.06	0.11	32
1260	89.8871	39.1572	94	3.3	0.65	0.04	0.07	36
1265	89.9385	39.1503	82	3.6	0.55	0.02	0.06	38
1270	89.9868	39.1385	94	6.0	0.60	0.05	0.12	36
1275	90.0396	39.1376	88	20.2	0.65	0.09	0.31	34
1285	90.1508	39.1115	86	6.0	0.75	0.11	0.18	31
1290	90.1913	39.0822	106	6.2	0.75	0.12	0.19	35
1295	90.2253	39.0589	88	5.3	0.50	0.09	0.15	37
1300	90.2143	39.0189	94	14.6	0.50	0.17	0.33	37
1310	90.1532	38.9382	174	10.2	0.60	0.20	0.31	31
1345	90.1673	38.6571	92	5.1	1.05	0.11	0.16	36
1400	90.3737	38.3263	82	18.2	0.60	0.11	0.31	30
1420	90.5832	38.3319	116	13.8	1.00	0.17	0.32	33
1430	90.6907	38.321	136	9.3	0.75	0.25	0.35	27
1465	90.9813	38.1263	22	24.4	0.25	0.09	0.36	32
AXX	95.81	40.41	82	4.0	0.50	0.07	0.11	291
DHT	94.81	40.03	46	2.8	0.50	0.03	0.06	215
GOM	94.81	36.20	100	3.2	1.15	0.16	0.19	251
LEH	93.41	38.82	142	4.4	0.55	0.07	0.12	203
RUQ	88.83	38.97	84	3.6	0.50	0.06	0.10	218
WTM	92.81	36.82	138	2.2	0.35	0.04	0.06	271

a) φ, fast direction; φ_{err}, measurement error of φ; δt, splitting time; δt_{err}, measurement error of δt; *SD*, standard deviation.

during the Paleoproterozoic (Yang et al., 2018). The TDF, which lies within the CTT, is marked by significant offsets in both the Moho and the Conrad discontinuities (Wu et al., 2024). These deep structural features suggest that this presently inactive fault may represent the Paleoproterozoic suture zone formed during the amalgamation. The ENE-WSW fast direction in this region aligns with the strike of the TDF. The consistency indicates that the crustal anisotropy likely originates from the lattice-preferred orientation of anisotropic minerals (e.g., amphibole) in the middle-lower crust—a fabric likely established during continental collision and oriented along the suture zone. Analogous to our findings, a preserved lithospheric fossil anisotropy has been documented in the Jiaodong Peninsula, East China. There, the crust and upper mantle anisotropy beneath the Wulian-Yantai Fault Zone aligns with the fault strike, reflecting deformation from the Late Triassic collision between the South China Block and the North China Craton (Wu et al., 2020, 2021). The crustal anisotropy within the South China Block also reflects the impacts

of ancient geological events. Its dominant NE-SW orientation is primarily caused by the lattice-preferred orientation of anisotropic minerals, a fabric developed during lithospheric extension as a consequence of the paleo-Pacific Plate subduction and rollback (Qian et al., 2025). However, such an extensional setting still persists at present, which is distinct from the fossil anisotropy.

The Cherchen Fault, situated in the southeastern Tarim Basin, is a large-scale inherited structure that separates the Paleozoic orogenic system along the Tibetan margin to the south from the contemporaneous Tarim Basin to the north (Laborde et al., 2019). Although strike-slip movement occurred along this fault in the Middle Miocene, it was confined to the western segment (Tian et al., 2023), while the eastern segment (this study area) shows no signs of reactivation. The crustal anisotropy observed parallel to the Cherchen Fault in its vicinity is thus interpreted as a relic of crustal deformation associated with this paleotectonic boundary.

The fast direction shifts from ENE-WSW to WNW-ESE between the Cherchen Fault and the Tadong Fault. The rotation may reflect the influence of the Tadong Uplift beneath the region—a prominent paleo-uplift structure within the Tarim Basin (Lin et al., 2012). Notably, significant uplift features are observed in both the sedimentary basement and the Conrad discontinuity (Wu et al., 2024; Xie et al., 2024). Comprehensive analysis of seismic and drilling data reveals that the Tadong Uplift records the strongest Paleozoic deformation of this region. This deformation event occurred during the Middle Devonian and was driven primarily by the collision between the Tianshan orogenic belt and the Tarim Block, which induced the internal deformation observed within the Tadong Uplift (Lin et al., 2012).

The crustal anisotropy shows obvious small-scale variations that preserve paleotectonic deformation characteristics. In contrast, the upper mantle anisotropy inferred from XKS phases exhibits a predominant NE-SW orientation, which diverges from crustal anisotropy pattern. This observed discrepancy indicates weak crust-mantle deformation coupling. Additionally, the significant divergence between the fast direction from XKS splitting analysis and that predicted by surface deformation field further supports the hypothesis of crust-mantle decoupled deformation (Chang and Wang, 2023). Meanwhile, Pn anisotropy reveals deformation in the uppermost mantle. At the eastern margin of the Tarim Basin, it shows a nearly N-S fast direction (Zhou and Lei, 2016), which deviates substantially from both crustal and upper mantle anisotropy. This observation not only verifies the occurrence of crust-mantle decoupling deformation but also reveals the complex lithospheric deformation pattern along the eastern margin of the Tarim Craton.

5.2 Transpressional deformation of the Altyn Tagh Range

A key finding of this research is the detection of near E-W oriented crustal anisotropy along the ATR northern edge (Fig. 5). This observation is supported by a high-resolution CCP image derived from our dense seismic array, which shows the southward underthrusting of the Tarim lower crust beneath the ATR. This underthrusting therefore drives upper crustal thickening and uplift of the ATR. The associated incorporation of felsic material thereby accounts for the reduced crustal Vp/Vs ratio (Wu et al., 2024). Driven by N-S compression, crustal materials

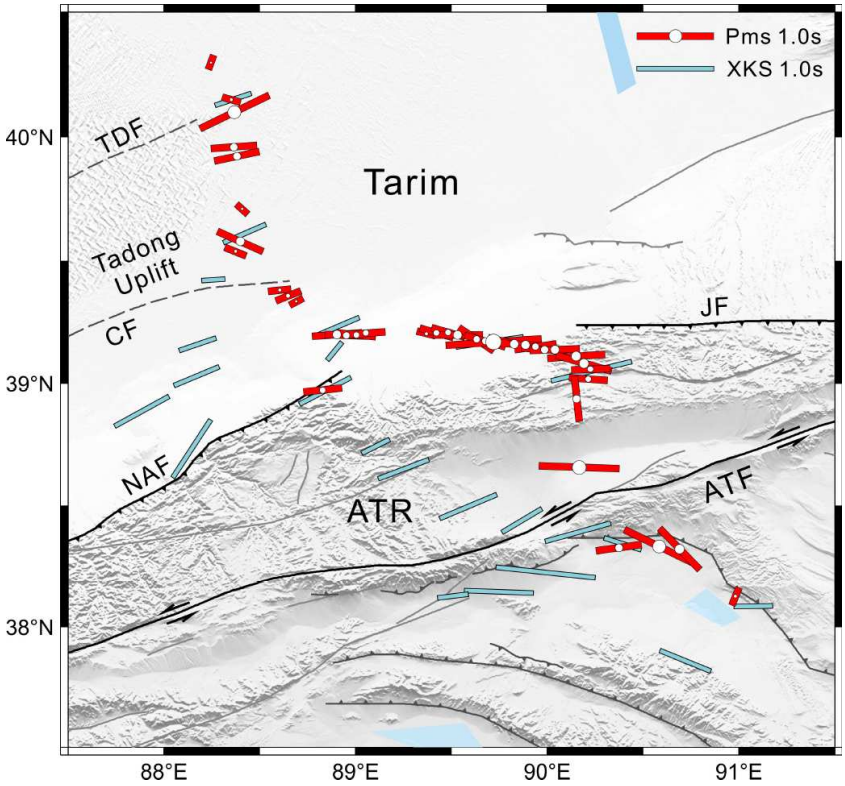

Fig. 5 Crustal anisotropy derived from the short-period dense array. Red bars show the fast direction (orientation) and splitting time (bar length) for the short-period array and permanent station RUQ. The central circle diameter scales with the splitting time. Blue bars denote previous upper mantle anisotropy measurements from XKS splitting in this region (Herquel et al., 1999; Guo et al., 2019; Chang and Wang, 2023).

deform via E-W pure shear. This process can establish a lattice-preferred orientation in anisotropic minerals like amphibole, generating the observed E-W crustal anisotropy—a mechanism analogous to the alignment of olivine in the upper mantle (Xu et al., 2018). At the surface, this tectonic process is manifested as major thrust faults—primarily the Jinyanshan Fault and the North Altyn Fault. Importantly, the crustal anisotropy is roughly parallel to the fast direction derived from XKS phases. This consistency indicates vertically coherent lithospheric deformation across the region, dominated by a pure shear mechanism. This interpretation is further validated by the work of Chang and Wang (2023), who reached a similar conclusion through analysis of XKS splitting and the surface deformation field.

The lower crust of the Tarim Block underthrusts beneath the ATR to a depth around 75 km (Wu et al., 2024). Here, partial eclogitization of the underthrust wedge and intense compression weaken the Pms phase, which impedes the estimation of anisotropy parameters at most stations. The only two successful measurements, from central stations 1345 and 1400, show fast directions parallel to the ATF strike, consistent with the ENE-WSW oriented mantle anisotropy from XKS phases. This parallelism implies vertically coherent lithospheric deformation, which can be attributed to simple shear deformation driven by rapid left-lateral motion along the central ATF. This process induces a coherent lattice-preferred orientation of anisotropic minerals throughout the crust and upper mantle. This coherent fabric indicates that the ATF acts as a through-going lithospheric fault (Wu et al., 2024; Yao et al., 2025). Further evidence comes from the southeastern side of the ATF (western Qaidam margin), where the crustal anisotropy abruptly rotates from ENE-WSW to WNW-ESE. The abrupt directional shift delineates that the ATF acts as a major, crust-penetrating tectonic boundary that separates two domains characterized by distinct deformation styles.

The southward underthrusting of the Tarim lower crust intersects the strike of the ATF at an oblique angle, establishing an oblique convergence regime along the boundary. This configuration results in transpressional deformation across the ATR, characterized by left-lateral simple shear (localized along the ATF) and pure shear (dominant at the northern boundary of the ATR). This oblique convergence directly promotes strike-slip motion along the ATF. The central segment of the ATF exhibits markedly larger crustal anisotropy than the eastern segment, with a maximum splitting time of 1.25 s and an average of 0.62 s, compared to the eastern average of about 0.50 s. This indicates more intense crustal underthrusting, which in turn corresponds to a rapid slip rate of approximately 10 mm yr^{-1} in the central ATF—far exceeding the rate of about 2 mm yr^{-1} observed in the eastern part (Li et al., 2018). Furthermore, in the eastern segment, the ENE-WSW oriented crustal anisotropy is nearly perpendicular to the NW-SE oriented upper mantle anisotropy inferred from XKS phases (Fig. 6), indicating crust-mantle decoupling (Guo et al., 2019). This decoupled state contrasts with the coupled deformation in the central segment, thereby revealing distinct deformation patterns along the strike of the ATF (Li et al., 2011).

5.3 Pure shear deformation of the Qaidam Block

The focal mechanism solutions transition from strike-slip type near the ATF to thrust type in the western Qaidam Basin, reflecting a change in crustal deformation mechanism (Yao et al., 2024). Correspondingly, this deformation is manifested as a series of WNW- to NW-striking thrust structures in the western Qaidam Basin, such as the Qaidam northern edge fault and the Qimantag Fault (Li et al., 2006; Huang et al., 2020). The far-field impacts of the India-Eurasia continental collision drive the NNE to NE extrusion of Tibetan Plateau material. This large-scale extrusion, in turn, facilitates left-lateral strike-slip along the ATF and induces NW-SE extensional deformation in the Qaidam

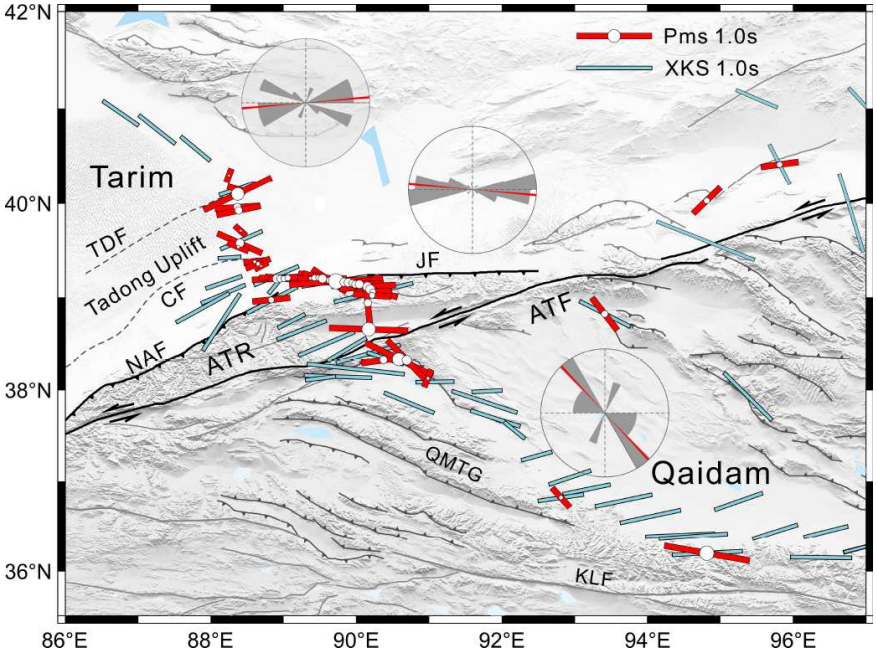

Fig. 6 Crustal anisotropy measurements derived from short-period and permanent stations. The legend follows Fig. 5. The three rose diagrams display the fast-direction distributions for the eastern Tarim, Altyn Tagh Range, and Qaidam regions, with red lines indicating their respective average fast directions.

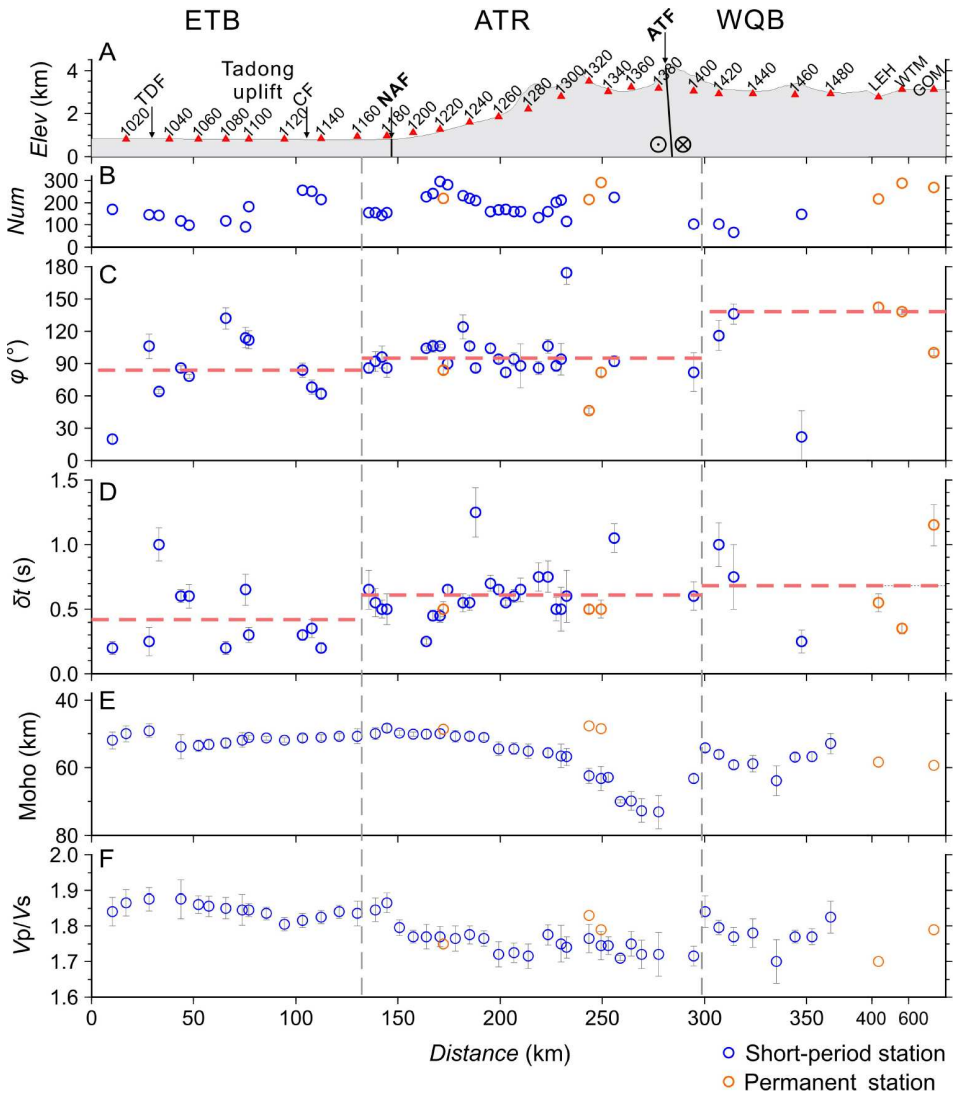

Fig. 7 Crustal anisotropy and *H*-*κ* results along the profile in Fig. 1B. Results from the short-period dense array and permanent stations are shown as blue and orange circles, respectively. (A) Station locations and topography. (B) Count of RFs used per station. (C, D) Fast directions and splitting times of crustal anisotropy with errors; the red dashed lines represent regional averages. (E, F) Moho depth and *Vp*/*Vs* ratio from *H*-*κ* scanning. Data in (E, F) originate from Wu et al. (2024) (blue circles) and He et al. (2014) (orange circles).

Basin. This process generated NW-SE crustal anisotropy parallel to the surface thrust faults (Figs. 6 and 7), indicating a pure-shear deformation pattern within the Qaidam crust. By integrating these results with those from the eastern Tarim Basin and the ATR, we reveal the crustal deformation pattern across the ATF system (Fig. 8). The oblique Tarim-Tibet convergence not only drives strike-slip motion along the central ATF but also accommodates NE extrusion of the plateau, thereby dominating the regional intracontinental deformation pattern.

The upper mantle deformation inferred from XKS splitting in the Qaidam Block shows distinct zonal characteristics (Chang and Wang, 2023). In the western Qaidam Basin, the WNW-ESE oriented upper mantle anisotropy is roughly parallel to the crustal anisotropy. The parallelism reflects the vertically coherent lithospheric deformation with crust-mantle coupling. By contrast, the ENE-WSW orientation of upper mantle anisotropy in the eastern basin is oblique to the crustal anisotropy (e.g., stations WTM, GOM), which suggests potential crust-mantle decoupling. The coupled deformation pattern in the western basin does not support the existence of middle-lower crustal flow in the region (Zhang et al., 2015). Although the middle-lower crust exhibits low velocity and electrical resistivity (Zhao et al., 2006; Zhang et al., 2015), the crustal flow model requires a *Vp*/*Vs* ratio of at least 1.80 (Liu et al., 2021), which is substantially above the measured regional average of 1.77 (Fig. 7; Wu et al., 2024). Furthermore, the NE-SW oriented anisotropy predicted by the plateau-outward flow (Klemperer, 2006) contradicts the observed WNW-ESE fast direction. However, it should be noted that the station coverage in the Qaidam Block is relatively sparse in this study, and more data are required to better constrain the crustal deformation features and the crust-mantle coupling pattern.

6. Conclusions

We derived crustal anisotropy beneath the central Altyn Tagh

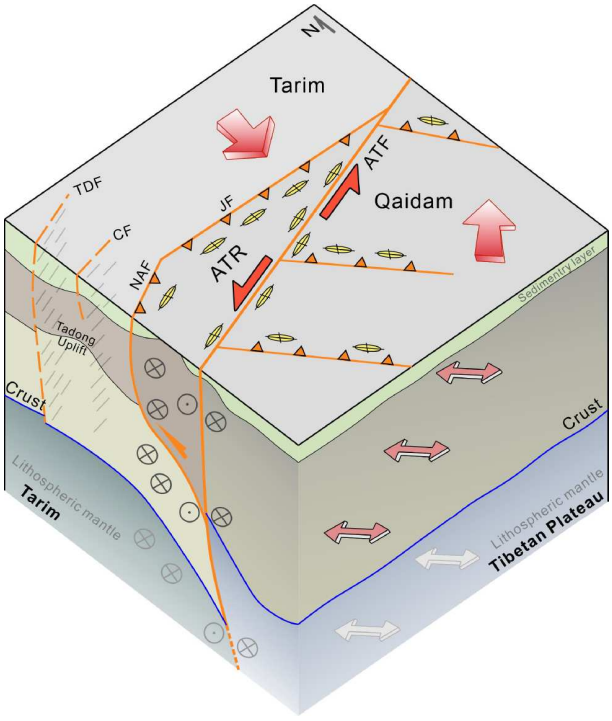

Fig. 8 Schematic diagram of intracontinental deformation patterns across the ATF system. Symbolism is as follows: red unidirectional arrows indicate block movements; half-arrows show the left-lateral motion of the ATF. Active and inherited (non-reactivated) faults are shown as solid and dashed orange lines, respectively; thrust faults are marked with triangles. The major axes of the yellow ellipses represent crustal anisotropy fast directions. Bidirectional arrows mark fast directions: red for crustal anisotropy and gray for upper mantle anisotropy. Paired circle-dots/crosses denote ATF strike-slip; other circle-crosses show lateral extensional extrusion in the Altyn Tagh Range. Gray short lines near the Tadong and Cherchen Faults represent fossil anisotropy in the Tarim crust. The Moho (deep blue lines) and crustal structure are from receiver function imaging (Wu et al., 2024).

Fault and its surroundings by analyzing the sinusoidal moveout of Pms phases in receiver functions. The resulting 43 pairs of anisotropy parameters predominantly reflect deformation within the middle-lower crust. Crustal anisotropy in the eastern Tarim Block is largely parallel to paleotectonic trends, reflecting fossil anisotropy of the ancient craton. The southward underthrusting of the Tarim Block and the NNE-NE extrusion of the Tibetan Plateau have induced pure-shear deformation within the crust beneath the northern Altyn Tagh Range and the western Qaidam Basin, respectively, generating corresponding E-W and NW-SE crustal anisotropy aligned with the regional thrust faults. The oblique convergence between the Tarim Block and the Tibetan Plateau has driven rapid strike-slip and left-lateral shearing in the central segment of the Altyn Tagh Fault. Integrated with upper-mantle deformation characteristics, these observations indicate crust-mantle decoupling in the eastern Tarim, whereas the Altyn Tagh Range and western Qaidam exhibit vertically coherent lithospheric deformation (Fig. 8).

Acknowledgement

We appreciate the support of the Geophysical Exploration Center, China Earthquake Administration for the field data acquisition. We thank Profs. Yang CHU, Youshan LIU and Lingtong MENG for constructive discussions. We are grateful to the Data Management Center of the China National Seismic Network at the Institute of Geophysics, China Earthquake Administration, for providing seismic data from permanent stations. This work was supported by the Strategic Priority Research Program of the Chinese Academy of Sciences (Grant No. XDA0430101) and the National Natural Science Foundation of China (Grant Nos. 42574124, 42404071, 42130807 & 42374063).

Compliance and ethics

The authors declare no conflict of interest.

References

Avouac J, Tapponnier P. 1993. Kinematic model of active deformation in central Asia. Geophys Res Lett, 20: 895–898

Chang L, Wang C. 2023. Teleseismic shear wave splitting and intracontinental collision deformation of the northern Tibetan Plateau and the eastern Tarim Basin. Sci China Earth Sci, 66: 1556–1568

Chen Y W, Li S H, Sun J, et al. 2013. OSL dating of offset streams across the Altyn Tagh Fault: Channel deflection, loess deposition and implication for the slip rate. Tectonophysics, 594: 182–194

Chen Y, Zhang Z, Sun C, et al. 2013. Crustal anisotropy from Moho converted Ps wave splitting analysis and geodynamic implications beneath the eastern margin of Tibet and surrounding regions. Gondwana Res, 24: 946–957

Cowgill E. 2007. Impact of riser reconstructions on estimation of secular variation in rates of strike-slip faulting: Revisiting the Cherchen River site along the Altyn Tagh Fault, NW China. Earth Planet Sci Lett, 254: 239–255

Cowgill E, Yin A, Harrison T M, et al. 2003. Reconstruction of the Altyn Tagh Fault based on U-Pb geochronology: Role of back thrusts, mantle sutures, and heterogeneous crustal strength in forming the Tibetan Plateau. J Geophys Res, 108: 2002JB002080

Efron B, Tibshirani R. 1986. Bootstrap methods for standard errors, confidence intervals, and other measures of statistical accuracy. Statist Sci, 1: 54–75

Gao Y. 2005. Studies on seismic anisotropy in the crust and mantle on Chinese mainland (in Chinese). Prog Geophys, 20: 180–185

Guo G, Zhang Z, Cheng J, et al. 2015. Seismic anisotropy in the crust in northeast margin of Tibetan Plateau and tectonic implication (in Chinese). Chin J Geophys, 58: 4092–4105

Guo G, Wu C, Tang G, et al. 2019. Seismic anisotropy of the northeastern margin of the Tibetan Plateau derived from analysis of SKS and Pms seismic phases (in Chinese). Chin J Geophys, 62: 1650–1662

He R, Shang X, Yu C, et al. 2014. A unified map of Moho depth and *Vp*/*Vs* ratio of continental China by receiver function analysis. Geophys J Int, 199: 1910–1918

Herquel G, Wittlinger G, Guilbert J. 1995. Anisotropy and crustal thickness of northern-Tibet. New constraints for tectonic modelling. Geophys Res Lett, 22: 1925–1928

Herquel G, Tapponnier P, Wittlinger G, et al. 1999. Teleseismic shear wave splitting and lithospheric anisotropy beneath and across the Altyn Tagh Fault. Geophys Res Lett, 26: 3225–3228

Huang X, Xu X, Gao R, et al. 2020. Shortening of lower crust beneath the NE Tibetan Plateau. J Asian Earth Sci, 198: 104313

Klemperer S L. 2006. Crustal flow in Tibet: Geophysical evidence for the physical state of Tibetan lithosphere, and inferred patterns of active flow. In: Law R D, Searle M P, Godin L, eds. Channel Flow, Ductile Extrusion, and Exhumation in Continental Collision Zones. London: Geological Society of London. 39–70

Kong F, Wu J, Liu K H, et al. 2016. Crustal anisotropy and ductile flow beneath the eastern Tibetan Plateau and adjacent areas. Earth Planet Sci Lett, 442: 72–79

Laborde A, Barrier L, Simoes M, et al. 2019. Cenozoic deformation of the Tarim Basin and surrounding ranges (Xinjiang, China): A regional overview. Earth-Sci Rev, 197: 102891

Li J, Song X, Wang P, et al. 2019. A generalized *H*-κ method with harmonic corrections on *Ps* and its crustal multiples in receiver functions. J Geophys Res Solid Earth, 124: 3782–3801

Li J, Gao Y, Wang Q. 2021. Anisotropic zoning in the upper crust of the Tianshan Tectonic Belt. Sci China Earth Sci, 64: 651–666

Li H, Yang J, Xu Z, et al. 2006. The constraint of the Altyn Tagh Fault system on the growth and rise of the northern Tibetan Plateau (in Chinese). Earth Sci Front, 13: 59–79

Li Y, Wu Q, Zhang F, et al. 2011. Seismic anisotropy of the Northeastern Tibetan Plateau from shear wave splitting analysis. Earth Planet Sci Lett, 304: 147–157

Li Y, Shan X, Qu C, et al. 2018. Crustal deformation of the Altyn Tagh Fault based on GPS. J Geophys Res Solid Earth, 123: 10309–10322

Ligorría J P, Ammon C J. 1999. Iterative deconvolution and receiver-function estimation. Bull Seismol Soc Am, 89: 1395–1400

Lin C, Yang H, Liu J, et al. 2012. Distribution and erosion of the Paleozoic tectonic unconformities in the Tarim Basin, Northwest China: Significance for the evolution of paleo-uplifts and tectonic geography during deformation. J Asian Earth Sci, 46: 1–19

Liu H, Niu F. 2012. Estimating crustal seismic anisotropy with a joint ana-

lysis of radial and transverse receiver function data. Geophys J Int, 188: 144–164
Liu Z, Tian X, Liang X, et al. 2021. Magmatic underplating thickening of the crust of the southern Tibetan Plateau inferred from receiver function analysis. Geophys Res Lett, 48: e2021GL093754
Nie S, Li J, Wu C, et al. 2023. Formation of the V-shaped conjugate strike-slip faults revealed by crustal anisotropy in the central Tibetan Plateau. J Asian Earth Sci, 258: 105725
Qian L, Lei J, Zhao D. 2025. Crustal anisotropy and deformation in the South China Block. J Asian Earth Sci, 289: 106627
Qiang Z, Wu Q, He J, et al. 2019. Crustal azimuthal anisotropy beneath Abag area in Inner Mongolia, China (in Chinese). Chin J Geophys, 62: 2946–2958
Rabbel W, Mooney W D. 1996. Seismic anisotropy of the crystalline crust: What does it tell us? Terra Nova, 8: 16–21
Rümpker G, Kaviani A, Latifi K. 2014. Ps-splitting analysis for multilayered anisotropic media by azimuthal stacking and layer stripping. Geophys J Int, 199: 146–163
Shen X, Yuan X, Ren J. 2015. Anisotropic low-velocity lower crust beneath the northeastern margin of Tibetan Plateau: Evidence for crustal channel flow. Geochem Geophys Geosyst, 16: 4223–4236
Shen Z, Wang M, Li Y, et al. 2001. Crustal deformation along the Altyn Tagh Fault system, western China, from GPS. J Geophys Res, 106: 30607–30621
Shi D, Yu Q, Poupinet G, et al. 2007. Crustal structures across the Altyn Tagh Fault imaged by teleseismic receiver functions and their geodynamic implications (in Chinese). Acta Geologica Sinica, 81: 139–144
Shi Y, Gao Y, Zhang H, et al. 2023. Crustal azimuthal anisotropy in the lateral collision zone of the SE margin of the Tibetan Plateau and its tectonic implications. Geophys J Int, 234: 1–11
Silver P G, Chan W W. 1991. Shear wave splitting and subcontinental mantle deformation. J Geophys Res, 96: 16429–16454
Sun S, Dong Y, Li Y, et al. 2024. Rheology of continental lithosphere and seismic anisotropy. Sci China Earth Sci, 67: 31–60
Sun Y, Niu F, Liu H, et al. 2012. Crustal structure and deformation of the SE Tibetan plateau revealed by receiver function data. Earth Planet Sci Lett, 349-350: 186–197
Tan P, Nie S. 2021. Crustal deformation in eastern margin of Tibetan Plateau from a dense linear seismic array. Phys Earth Planet Inter, 321: 106801
Tan P, Liang X, Li W, et al. 2023. Crustal structure of the Tibetan Plateau and adjacent areas revealed from ambient noise tomography. Gondwana Res, 121: 1–15
Tapponnier P, Molnar P. 1977. Active faulting and tectonics in China. J Geophys Res, 82: 2905–2930
Tapponnier P, Zhiqin X, Roger F, et al. 2001. Oblique stepwise rise and growth of the Tibet Plateau. Science, 294: 1671–1677
Tian H, Chen H, Cheng X, et al. 2023. Limited northward expansion of the Tibetan Plateau in the Late Cenozoic: Insights from the Cherchen Fault in the Southeastern Tarim Basin. Tectonics, 42: e2022TC007694
Wang C, Mooney W D, Wang X, et al. 2024. Intra-continental collision of the Tarim Basin and the Northern Tibetan Plateau. J Geophys Res Solid Earth, 129: e2024JB028668
Wang D, Zhao B, Yu J, et al. 2020. Active tectonic deformation around the Tarim Basin inferred from dense GPS measurements. Geodesy Geodyn, 11: 418–425
Wang Q, Niu F, Gao Y, et al. 2016. Crustal structure and deformation beneath the NE margin of the Tibetan plateau constrained by teleseismic receiver function data. Geophys J Int, 204: 167–179
Wang Y, Zheng J, Zhang W, et al. 2012. Cenozoic uplift of the Tibetan Plateau: Evidence from the tectonic-sedimentary evolution of the western Qaidam Basin. Geosci Front, 3: 175–187
Wittlinger G, Tapponnier P, Poupinet G, et al. 1998. Tomographic evidence for localized lithospheric shear along the Altyn Tagh Fault. Science, 282: 74–76
Wu C, Tian X, Xu T, et al. 2019. Deformation of crust and upper mantle in central Tibet caused by the northward subduction and slab tearing of the Indian lithosphere: New evidence based on shear wave splitting measurements. Earth Planet Sci Lett, 514: 75–83
Wu C, Xu T, Ai Y, et al. 2020. XKS splitting-based upper-mantle deformation in the Jiaodong Peninsula records the boundary between the North China Craton and South China Block. Geophys J Int, 222: 956–964
Wu C, Xu T, Ai Y, et al. 2021. Crustal azimuthal anisotropy in the Jiaodong Peninsula: Evidence for the suture between the North China Craton and South China Block. Phys Earth Planet Inter, 314: 106705
Wu C, Xu T, Bai Z. 2023. Detailed crustal deformation in the Ailaoshan Orogenic Belt revealed by receiver functions from a dense array. Front Earth Sci, 11: 1343474
Wu C, Xu T, Tian X, et al. 2024. Underthrusting of Tarim lower crust beneath the Tibetan Plateau revealed by receiver function imaging. Geophys Res Lett, 51: e2024GL108220
Wu J, Zhang Z, Kong F, et al. 2015. Complex seismic anisotropy beneath western Tibet and its geodynamic implications. Earth Planet Sci Lett, 413: 167–175
Wu L, Lin X, Cowgill E, et al. 2019. Middle Miocene reorganization of the Altyn Tagh Fault system, northern Tibetan Plateau. GSA Bull, 131: 1157–1178
Xie T, Xu T, Yang Y, et al. 2023. Observation of higher-mode rayleigh waves from ambient noise in the Tarim Basin, China. Seismological Res Lett, 94: 1848–1859
Xie T, Yang Y, Xu T, et al. 2024. 2-D sedimentary structures at the southeast margin of the Tarim Basin, China, constrained by Love wave ambient noise tomography. Geophys J Int, 239: 1775–1788
Xu X, Niu F, Ding Z, et al. 2018. Complicated crustal deformation beneath the NE margin of the Tibetan plateau and its adjacent areas revealed by multi-station receiver-function gathering. Earth Planet Sci Lett, 497: 204–216
Xu Y G, Wei X, Luo Z Y, et al. 2014. The Early Permian Tarim Large Igneous Province: Main characteristics and a plume incubation model. Lithos, 204: 20–35
Yang H, Wu G, Kusky T M, et al. 2018. Paleoproterozoic assembly of the North and South Tarim terranes: New insights from deep seismic profiles and Precambrian granite cores. Precam Res, 305: 151–165
Yang W, Wang J, Zhong H, et al. 2012. Analysis of regional magnetic field and source structure in Tarim Basin (in Chinese). Chin J Geophys, 55: 1278–1287
Yang Y, Zhang X, Dong Y, et al. 2022. Crustal deformation patterns in the Tibetan Plateau and its adjacent regions as revealed by receiver functions. Bull Seismol Soc Am, 112: 1297–1314
Yao S, Xu T, Sang Y, et al. 2024. The seismicity in the middle section of the Altyn Tagh Fault system revealed by a dense nodal seismic array. Earthquake Res Adv, 4: 100308
Yao S, Xu T, Yang T, et al. 2025. Lithospheric structure of the central Altyn Tagh Fault system revealed by teleseismic travel-time tomography. Seismological Res Lett, 96: 2300–2310
Yin A, Harrison T M. 2000. Geologic evolution of the Himalayan-Tibetan orogen. Annu Rev Earth Planet Sci, 28: 211–280
Yin A, Rumelhart P E, Butler R, et al. 2002. Tectonic history of the Altyn Tagh Fault system in northern Tibet inferred from Cenozoic sedimentation. Geol Soc Am Bull, 114: 1257–1295
Yue Y, Liou J G. 1999. Two-stage evolution model for the Altyn Tagh Fault, China. Geology, 27: 227–230
Zhang B, Bao X, Xu Y. 2022. Seismic anisotropy in the central Tien Shan unveils rheology-controlled deformation during intracontinental orogenesis. Geology, 50: 812–816
Zhang B, Bao X, Wu Y, et al. 2023. Southern Tibetan rifting since late Miocene enabled by basal shear of the underthrusting Indian lithosphere. Nat Commun, 14: 2565
Zhang L, Unsworth M, Jin S, et al. 2015. Structure of the Central Altyn Tagh Fault revealed by magnetotelluric data: New insights into the structure of the northern margin of the India-Asia collision. Earth Planet Sci Lett, 415: 67–79
Zhang P, Molnar P, Xu X. 2007. Late Quaternary and present-day rates of slip along the Altyn Tagh Fault, northern margin of the Tibetan Plateau. Tectonics, 26: 2006TC002014
Zhao J, Mooney W D, Zhang X, et al. 2006. Crustal structure across the Altyn Tagh Range at the northern margin of the Tibetan Plateau and tectonic implications. Earth Planet Sci Lett, 241: 804–814
Zheng T, Ding Z, Ning J, et al. 2018. Crustal azimuthal anisotropy beneath the Southeastern Tibetan Plateau and its geodynamic implications. J Geophys Res Solid Earth, 123: 9733–9749
Zhou Z, Lei J. 2016. Pn anisotropic tomography and mantle dynamics beneath China. Phys Earth Planet Inter, 257: 193–204

(Editorial handling: Dinghui YANG)